Growth of ferromagnetic nanoparticles in a diluted magnetic semiconductor obtained by Mn^+ implantation on Ge single crystals

M. Passacantando, L. Ottaviano, F. D'Orazio, and F. Lucari
Dipartimento di Fisica and INFM, Università di L'Aquila, I-67010 Coppito (L'Aquila), Italy

M. De Biase
Via Madonna Fore 23, I-67100 L'Aquila, Italy

G. Impellizzeri and F. Priolo
MATIS-INFM and Dipartimento di Fisica e Astronomia, Università di Catania, I-95123 Catania, Italy
(Received 21 March 2006; published 24 May 2006)

We used transmission electron microscopy and magneto-optical Kerr effect measurements to investigate the chemical, structural, and magnetic properties of MnGe alloys fabricated by ion implantation of Mn^+ at doses of 1×10^{16}, 2×10^{16}, and 4×10^{16} at./cm^2 on Ge(100) single crystals at a substrate temperature of 300 °C. Transmission electron microscopy images show the presence of Mn-rich clusters buried in a crystalline Ge matrix. These clusters are either Mn_5Ge_3 crystallites (with mean diameters of 9.5 and 13.1 nm for the samples implanted at 2×10^{16} and 4×10^{16} at./cm^2 doses, respectively) or in an amorphous phase (with average diameters of 4.3, 6.6, and 7.5 nm for the samples implanted at 1×10^{16}, 2×10^{16}, and 4×10^{16} at./cm^2 doses, respectively). Chemical maps obtained by electron energy loss spectroscopy reveal also the presence of manganese diluted in the host Ge matrix. The samples with higher doses are ferromagnetic with the Curie temperature approaching 270 K. The sample implanted at the 1×10^{16} at./cm^2 dose exhibits ferromagnetic hysteresis only at 5 K.

DOI: 10.1103/PhysRevB.73.195207 PACS number(s): 75.50.Pp, 61.72.Tt, 75.50.Kj, 81.07.Bc

Hybrid magnetic semiconductor materials of low dimensions are of great relevance in fundamental research and technological applications involving spintronic device developments.[1–5] Although most experimental work on ferromagnetic semiconductors has focused on III-V and II-VI compounds, there is broad interest in the group-IV semiconductors, C, Si, Ge, and $Si_{1-x}Ge_x$, owing to their potential compatibility with current Si-based processing technology.

Most of the current studies deal with diluted phases grown by molecular beam epitaxy (MBE). Low-temperature epitaxial growth has been used with Mn-doped GaAs (Ref. 6) achieving ferromagnetism with a transition temperature of 110 K, which is remarkably high compared to traditional dilute magnetic semiconductor (DMS) materials. More recently, ferromagnetism has been reported at temperatures above 300 K for $(Cd_{0.95}Mn_{0.05})GeP_2$ (Ref. 7), $Zn_{1-x}Mn_xGeP_2$ (Refs. 8 and 9), GaMnN (Refs. 10 and 11), GaMnP (Ref. 12), Co-TiO_2 (Refs. 13 and 14), and $ZnSnAs_2$ (Ref. 15). Some articles about Ge-based diluted magnetic semiconductors were presented in the past years. Park *et al.*[16] reported on the epitaxial growth of Mn_xGe_{1-x} by MBE, in which the Curie temperature (T_C) is found to increase linearly with Mn concentration from 25 to 116 K. The Mn dilution in Ge substrate is strongly dependent on the substrate temperature during the MBE growth, and already at 85 °C it has been shown that the films become strongly ferromagnetic (FM) with a T_C of 296 K due to the formation of Mn_5Ge_3 precipitates.[17] Moreover, it has been reported phase separation in Mn-rich precipitates with diameters of the same order of the typical film thicknesses for Mn_xGe_{1-x} samples grown by MBE at a substrate temperature $T\geqslant250$ °C (Ref. 18).

In this paper, we show that ion implantation is by far more effective for Mn dilution into Ge. We show that Mn doping of Ge results in the formation of ferromagnetic nanoparticles, some in a crystalline phase and some in an amorphous phase, with different size distributions (that vary from 4 to 13 nm) depending on the implanted dose. A coexistence of a DMS phase, previously indirectly evidenced with x-ray diffraction (XRD) and x-ray photoemission spectroscopy (XPS) on the same samples,[19] is here directly demonstrated. These alloys are ferromagnetic up to 270 K.

The samples were prepared by implanting Mn^+ on commercially purchased single-crystal Ge(100) wafers ($\rho=40-57\ \Omega$ cm). Mn^+ ions were implanted with an energy of 100 keV at doses of 1×10^{16}, 2×10^{16}, and 4×10^{16} at./cm^2. The three samples so obtained will be denoted A, B, and C, respectively. These doses produce an average volume concentration of about 3, 6, and 12 at. %, respectively, on top of the Ge substrate.[19] During the implantation, the samples were held at 300 °C to avoid amorphization. The depth projected range[20] (Rp) of Mn ions was estimated to be 57 nm with the implant designed to yield a quasi-Gaussian profile.

The structure of the implanted region and the characteristics of the nanoclusters populations were determined from transmission electron microscopy (TEM), high-resolution TEM (HRTEM), and elemental mapping of Mn atoms.

The magnetic characterization of the samples was obtained by magneto-optical Kerr effect (MOKE) measurements. The experiments were carried out at temperatures between 5 and 300 K using near-infrared radiation of 2 μm, incident with *s* polarization at an angle of 45° with respect to the sample surface. Since germanium is transparent at this wavelength, this assured that the whole MnGe implanted

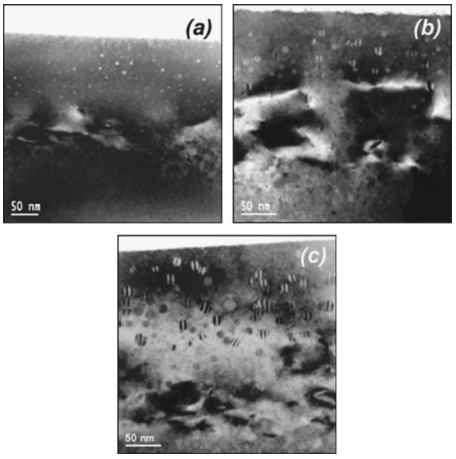

FIG. 1. Bright-field cross-sectional TEM images of the samples implanted at a dose of (a) 1×10^{16}, (b) 2×10^{16}, and (c) 4×10^{16} at./cm^2.

layer was tested by the experimental technique. Polar and longitudinal geometry gave similar trends as a function of temperature, indicating that no particular easy magnetization axis was present in the samples.

Figures 1(a)–1(c) are bright-field cross-sectional TEM images of the Mn-Ge implanted layer of the samples A, B, and C, respectively. The images show a fine dispersion of nanometer-size particles embedded in the Ge matrix. The population of the nanoclusters extends up to a depth, below the surface, of about 130 nm for samples A and B, and 140 nm for sample C, in agreement with the XPS depth profile reported in Ref. 19. Extended defects, induced by the implantation damage, are visible up to depths of 220, 240, and 280 nm for the samples A, B, and C, respectively.

The presence of the Moirè fringes in Figs. 1(b) and 1(c) indicates that some of the nanoparticles are in a crystalline phase. By increasing the Mn dose, we can observe an increase of the number of the particles with Moirè fringes. The orientation of these fringes is not random, since they are almost all perpendicular to the surface. This indicates that in average they are in the same register with the Ge matrix.

The mean diameter of the nanoclusters and their density are extracted from the TEM images. Table I summarizes the TEM results for the particle dimensions and the relative fraction of the total volume occupied by amorphous and crystalline particles. The general trend is that, by increasing the Mn dose, the mean particle size increases (see Table I for details). In particular, we obtain a mean diameter of 9.5 and 13.1 nm for the crystalline phase of samples B and C, respectively. A comparison with the work of Park *et al.*[18] is worthwhile. They reported, for Mn_xGe_{1-x} samples grown by MBE at substrate temperatures ranging from 250 to 350 °C, a formation of Mn-rich precipitate with an average size (100 nm) one order of magnitude larger than the typical values observed in our case.

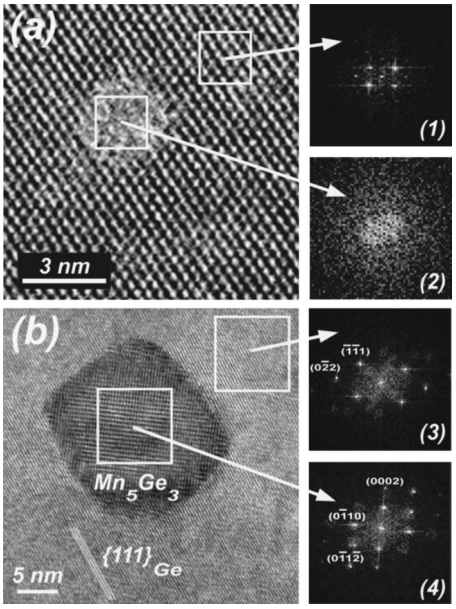

FIG. 2. HRTEM image, with the electron beam along the [011] direction, of the samples implanted at a dose of 1×10^{16} (a) and 4×10^{16} at./cm^2 (b). In the right panels, the fast Fourier transform of the square regions are reported; they identify the reciprocal lattice of the Ge matrix [panels (1) and (3)] and of the nanoparticles [panels (2) and (4)].

Figures 2(a) and 2(b) are HRTEM images of samples A and C, respectively, showing the Ge matrix and the embedded clusters. The direction of the electron beam referred to the Ge crystalline structure is [011] in both cases. It is already evident from the direct space TEM images that the host matrix has a good overall crystallinity, as shown in Fig. 2(b), where the {111} planes of the matrix are identified. This is also confirmed by the fast Fourier transforms (FFT) of the

TABLE I. Implantation conditions and measured parameters of the Mn-rich particles in the samples.

		Particle diameter (nm)				Particle volume (%)	
		Amorphous phase (D_A)		Crystalline phase (D_C)			
Sample	Mn implanted dose (at./cm^2)	mean	standard deviation	mean	standard deviation	Amorphous phase (V_A)	Crystalline phase (V_C)
A	1×10^{16}	4.3	1.3			100	
B	2×10^{16}	6.6	1.8	9.5	1.1	51	49
C	4×10^{16}	7.5	3.1	13.1	2.7	15	85

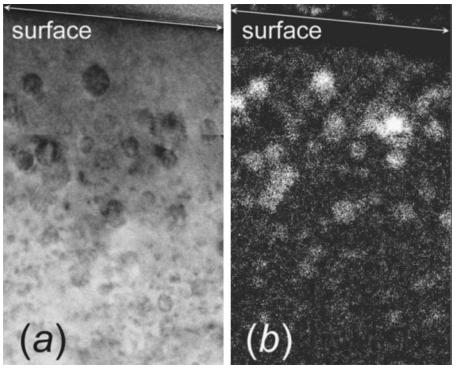

FIG. 3. EELS elemental mapping of Mn in Ge of the sample implanted at a dose of 4×10^{16} at./cm^2. Panels (a) and (b) show the plasmon loss image and EELS elemental mapping taken at the Mn L_3 edge, respectively. Bright regions in (b) correspond to higher Mn content.

Ge cubic structure near the [011] zone axis, shown in panels (1) and (3) of Fig. 2.

The particles without Moiré fringes in Figs. 1(a)–1(c) reveal a HRTEM image as the one reported in Fig. 2(a). There is no crystalline order inside such clusters [see also the FFT in panel (2) of Fig. 2]. On the other hand, a crystalline order is found in some clusters of samples B and C, as shown for the latter case in Fig. 2(b). Using the FFT image of the cluster crystal phase, shown in panel (4), we can ascertain that it represents a diffraction pattern for an hcp structure in the $[2\bar{1}\bar{1}0]$ beam direction. Moreover, we can determine the interplanar spacing corresponding to the reciprocal lattice points indexed in panel (4): we find 3.64, 2.53, and 2.06 Å, for the planes $(0\bar{1}10)$, (0002), and $(0\bar{1}\bar{1}2)$, respectively. These values are in excellent agreement with the corresponding theoretical distances (3.60, 2.53, and 2.07 Å, respectively) for the Mn_5Ge_3 compound, with unit-cell parameters: $a=b=7.18$ Å and $c=5.05$ Å (Ref. 21). Comparing panels (3) and (4) of Fig. 2, we observe that the $(001)_{Ge}$ plane is parallel to the $(0002)_{Mn_5Ge_3}$ plane. This result, together with the parallelism of the directions $[011]_{Ge}$ and $[2\bar{1}\bar{1}0]_{Mn_5Ge_3}$, uniquely determines the orientation of the Mn_5Ge_3 crystal structure with respect to the substrate Ge matrix. Similar results were obtained for the crystalline clusters of sample B. It follows that the c axis of Mn_5Ge_3 is perpendicular to the Ge(100) plane. This hypothesis is confirmed by XRD measurements performed on the same samples (B and C), in which we see only the (0002) and (0004) reflections of Mn_5Ge_3 in the Bragg–Brentano geometry.[19] On the contrary, no features are obtained in XRD grazing incidence mode (at an incident angle of 0.5°), indicating a crystallization of the nanoparticles with well-oriented (0002) planes.

Energy dispersive x-ray spectroscopy data were obtained from several locations of the samples (not shown). From these measurements it is not clear whether the Mn is present only in the precipitates or is also diluted in the matrix.

For this reason, we have analyzed sample C by means of electron energy loss spectroscopy (EELS). Figure 3 shows the plasmon loss image (a) and the EELS elemental mapping (b) taken at the Mn L_3 edge. The plasmon loss image shows a population of dark spots dispersed in the brighter matrix. The size distribution of these dark spots allows us to make a one-to-one correspondence between these spots and the populations of the Mn_5Ge_3 particles observed in Fig. 1(c). Consistent with this assignment, the particles are metallic (higher plasmon loss intensity). The Mn presence in the clusters is directly evidenced in the corresponding EELS image of Fig. 3(b). Beside the obvious high Mn content of the clusters, there is a significant Mn EELS signal also from the surrounding Ge matrix. Close to the surface, where there is no efficient Mn implantation, the EELS image is dark. On the contrary, more deeply in the sample, there is a diffuse brighter background that can be assigned to Mn not belonging to precipitates. In summary, we have here direct evidence of the coexistence of the Mn_5Ge_3 precipitates and diluted Mn in the host Ge matrix, already indirectly evidenced in Ref. 19.

EELS measurements were also performed on the other samples. In particular, the nanoclusters in sample A are also Mn-rich precipitates. Since this sample differs from the others in the implanted dose, obtained with a shorter implantation time, we can consider the clusters in A as precursors of the clusters in B and C, and we expect them to be in an amorphous Mn-rich phase. Presumably, a critical cluster size and Mn concentration must be reached in order to trigger the formation of the crystalline phase.

Saturation, remanence, and coercivity were obtained from the polar MOKE hysteresis loops using a phenomenological fitting similar to the one described elsewhere.[22] Figure 4(a) reports the polar loop of sample A at 5 K. In this case the amplitude of the Kerr signal is extremely small even at the lowest temperature. Moreover, the coercivity rapidly disappears as the temperature is raised, since it is undetectable at 12 K, although a weak saturation is found up to about 200 K. This magnetic behavior is in quantitative agreement with the one reported for MBE-grown MnGe alloys, with comparable Mn concentration, where the effective Mn dilution in the Ge matrix is clearly assessed;[17] although, recently, Sugahara *et al.*, in a similar MBE film, attributed the magnetic response to the presence of amorphous semiconducting Mn-rich precipitates.[23]

Figure 4(b) reports the polar loops of samples B and C at 100 K. Clearly, these samples show much higher magneto-optical signal and a stronger hysteresis with respect to sample A. Comparing the loops shown in the figure, we notice that the Kerr rotation scales approximately with the Mn content. Moreover, we notice a different shape of the loops, i.e., a larger coercivity and squareness of sample C; a feature that is maintained at all the other temperatures investigated. For both samples the remanence and the coercivity remain up to almost room temperature [Figs. 4(c) and 4(d)]. The values of T_C estimated from the temperature dependence of these two parameters are about 255 and 270 K for samples B and C, respectively. Notice that the initial increase of remanence with temperature for sample C in Fig. 4(c) is only apparent due to the limited range of magnetic fields available: at low temperature, when the irreversible field exceeds the maximum field of the measurement apparatus, we obtain minor loops. The dashed line in the figure represents qualitatively the expected remanence that would be obtained from a major loop.

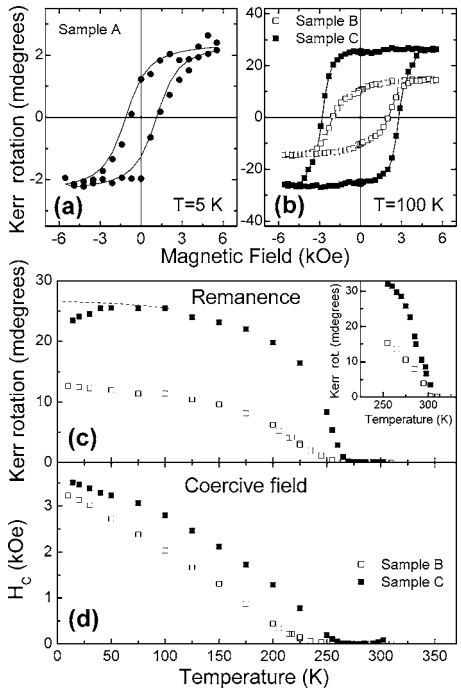

FIG. 4. Polar MOKE hysteresis loops: (a) at 5 K of sample A, implanted at a dose of 1×10^{16} at./cm^2; (b) at 100 K of samples B (□) and C (■), implanted at a dose of 2×10^{16} and 4×10^{16} at./cm^2, respectively. Temperature dependence of the MOKE remanence (c) and coercive field (d) for the samples B and C. The dashed line in (c) represents the extrapolated low-temperature remanence from major loops of sample C (see comment in the text). In the inset of panel (c) part of the temperature dependence of the MOKE saturation for samples B (□) and C (■) are also shown.

The different magnetic response of the two samples revealed in Figs. 4(b)–4(d), in particular the higher coercive field reported in the latter figure, indicates a larger magnetocrystalline anisotropy of sample C. This may be attributed to the larger size of its particles, to the higher relative amount of crystalline particles, and to the higher overall Mn concentration. In this respect, the preferential orientation of the Mn_5Ge_3 crystallites may play an important role, since the [0001] direction of that structure results in an easy magnetization axis which would provide an out-of-plane component to the resulting anisotropy, balancing the in-plane contribution from the film shape anisotropy expected for a long-range interaction among the particles. This justifies the aforementioned observed similar polar and longitudinal MOKE experimental results. Actually, it is possible that not only the Mn_5Ge_3 particles, but also the diluted Mn region, contribute to the MOKE signal. Likely, the presence of the magnetic particles embedded in the DMS enhances the long-range magnetic order of the DMS matrix, increasing its Curie temperature and the squareness of the hysteresis loops. Clearly, the two phases have a single cooperative magnetic response. A similar interpretation was also given for the observed inhomogeneously distributed Mn in MBE-grown Ge:Mn alloys.[24]

In the inset of Fig. 4(c) we report the high-temperature portion of the saturation. It is evident that the samples manifest a magnetic character also above T_C, up to about 300 K. This value is very close to the reported Curie temperature T_C^* of Mn_5Ge_3 (Ref. 25) suggesting, for $T_C<T<T_C^*$, the loss of strong interactions among the Mn_5Ge_3 particles, leaving them in a super-paramagnetic state.

In conclusion, we have demonstrated that implantation of Mn ions in a Ge matrix generates Mn-rich clusters embedded in a diluted Mn-Ge semiconducting matrix. The choice of the implanted dose of ions affects the number and dimension of the particles, their compositional and crystalline character, and the relative amount of Mn located in the cluster or in the matrix. In turn, these factors influence the magnetic response of the system. The control of the other implantation parameters (energy, temperature, and rate) may also affect the resulting structural and magnetic properties of the compound. This opens a wide playground for further investigations in the field of magnetic semiconductors.

[1] S. A. Wolf, J. Supercond. **13**, 195 (2000).
[2] G. A. Prinz, Science **282**, 1660 (1998).
[3] J. K. Furdyna, J. Appl. Phys. **64**, R29 (1988).
[4] S. Gopalan and M. G. Cottam, Phys. Rev. B **42**, 10311 (1990).
[5] C. Haas, CRC Crit. Rev. Solid State Sci. **1**, 47 (1970).
[6] H. Ohno, Science **281**, 951 (1998).
[7] G. Medvedkin, T. Ishibaski, T. Niski, K. Hayata, Y. Hasagawa, and K. Sata, Jpn. J. Appl. Phys., Part 2 **39**, L949 (2000).
[8] G. A. Medvedkin, K. Hirose, T. Ishibashi, T. Nishi, V. G. Voevodin, and K. Sato, J. Cryst. Growth **236**, 609 (2002).
[9] S. Cho, S. Choi, G.-B. Cha, S. C. Hong, Y. Kim, Y.-J. Zhao, A. J. Freeman, J. B. Ketterson, B. J. Kim, Y. C. Kim, and B.-C. Choi, Phys. Rev. Lett. **88**, 257203 (2002).
[10] M. L. Reed, N. A. El-Masry, H. N. Stadelmaier, M. K. Ritums, M. J. Reed, C. A. Parker, J. C. Roberts, and S. M. Bekair, Appl. Phys. Lett. **79**, 3473 (2001).
[11] G. T. Thaler, M. E. Overberg, B. Gila, R. Frazier, C. R. Abernathy, S. J. Pearton, J. S. Lee, S. Y. Lee, Y. D. Park, Z. G. Kim, J. Kim, and F. Ren, Appl. Phys. Lett. **80**, 3964 (2002).
[12] N. Theodoropoulou, A. F. Hebard, M. E. Overberg, C. R. Abernathy, S. J. Pearton, S. N. G. Chu, and R. G. Wilson, Phys. Rev. Lett. **89**, 107203 (2002).
[13] S. A. Chambers, S. Thevuthasan, R. F. C. Farrow, R. F. Marks, J. U. Thiele, L. Folks, M. G. Samant, A. J. Kellock, N. Ruzycki, D. L. Ederer, and U. Diebold, Appl. Phys. Lett. **79**, 3467 (2001).
[14] Y. Matsumoto, M. Murakami, T. Shono, T. Hasegawa, T. Fukumaura, M. Kawasaki, P. Ahmet, T. Chikyow, S. Koshihara, and H. Koinuma, Science **291**, 854 (2001).
[15] S. Choi, G. B. Cha, S. C. Hong, S. Cho, Y. Kim, J. B. Ketterson, S. Y. Jeong, and G. C. Yi, Solid State Commun. **122**, 165 (2002).
[16] Y. D. Park, A. T. Hanbicki, S. C. Erwin, C. S. Hellberg, J. M.

Sullivan, J. E. Mattson, T. F. Ambrose, A. Wilson, G. Spanos, and B. T. Jonker, Science **295**, 651 (2002).
[17] A. P. Li, J. Shen, J. R. Thompson, and H. H. Weitering, Appl. Phys. Lett. **86**, 152507 (2005).
[18] Y. D. Park, A. Wilson, A. T. Hanbicki, J. E. Mattson, T. Ambrose, G. Spanos, and B. T. Jonker, Appl. Phys. Lett. **78**, 2739 (2001).
[19] L. Ottaviano, M. Passacantando, S. Picozzi, A. Continenza, R. Gunnella, A. Verna, G. Bihlmayer, G. Impellizzeri, and F. Priolo, Appl. Phys. Lett. **88**, 061907 (2006).
[20] J. F. Zigler, J. P. Biersack, and U. Littmark, in *The Stopping and Range of Ions in Matter* (Pergamon, New York, 1985).
[21] JCPDS-ICDD card n. 6–646.
[22] F. D'Orazio, F. Lucari, M. Melchiorri, C. de Julián Fernández, G. Mattei, P. Mazzoldi, C. Sangregorio, D. Gatteschi, and D. Fiorani, J. Magn. Magn. Mater. **262**, 111 (2003).
[23] S. Sugahara, K. L. Lee, S. Yada, and M. Tanaka, Jpn. J. Appl. Phys., Part 2 **44**, L1426 (2005).
[24] N. Pinto, L. Morresi, M. Ficcadenti, R. Murri, F. D'Orazio, F. Lucari, L. Boarino, and G. Amato, Phys. Rev. B **72**, 165203 (2005).
[25] C. Zeng, S. C. Erwin, L. C. Feldman, A. P. Li, R. Jin, Y. Song, J. R. Thompson, and H. H. Weitering, Appl. Phys. Lett. **83**, 5002 (2003).